JOURNAL OF MATERIALS SCIENCE 32 (1997) 389–400

Electrochemical Al_2O_3–ZrO_2 composite coatings on non-oxide ceramic substrates

R. CHAIM, I. ZHITOMIRSKY*, L. GAL-OR*
*Department of Materials Engineering and *Israel Institute of Metals, Technion-Israel Institute of Technology, Haifa 32000, Israel*

H. BESTGEN
Hoechst AG, ZF-Methodische Projekts, Elektronenmikroskopie, 65926 Frankfurt/Main, Germany

Aqueous solutions of $xAl(NO_3)_3 + (1 - x)ZrO(NO_3)_2$ were used for electrodeposition of ceramic Al_2O_3–ZrO_2 composite coatings on TiC, TiB_2 and SiC substrates. The weight of the deposit was studied versus the duration of deposition, the current density and the temperature of the bath for Al-rich ($x = 0.9$), Zr-rich ($x = 0.4$) and eutectic ($x = 0.75$) electrolyte compositions. Optimal current densities and durations of deposition were determined to obtain maxima weights of deposits. Amorphous deposits with thicknesses up to 10 μm were formed. The microstructure and microchemical composition of the as-deposited and sintered deposits were characterized. Increase in the temperature of the bath inhibited microcracking due to shrinkage during drying. Coated TiC substrates exhibited enhanced oxidation resistance in air at 1100 °C.

1. Introduction

Electrochemical deposition of ceramic oxide coatings on semiconducting and ceramic substrates is a relatively new technique. This technique was used for deposition of monolithic zirconia [1–5], alumina [5, 6], chromia [7], as well as multilayer and semiconducting materials [8, 9]. For the formation of more complex binary or ternary systems one may take advantage of the solubility of various metal salts that act as precursors in an aqueous medium, in order to electrodeposit oxide alloys as well as oxide composites with homogeneously distributed oxide constituents.

Different compositions in the alumina–zirconia system are developed as advanced engineering ceramics, with improved toughness and strength. These include Zr-rich alloys (alumina toughened zirconias, ATZs) [10, 11], Al-rich alloys (zirconia toughened aluminas, ZTAs) [11–13], as well as alloys with eutetic composition [14, 15]. In this work, these three types of oxides are deposited as coatings on non-oxide substrates by electrodeposition. The electrochemical parameters and the microstructural evolution after sintering are characterized and discussed.

2. Experimental procedure

Commercially pure zirconyl-nitrate-hydrate $[ZrO(NO_3)_2 \cdot nH_2O$ and aluminum-nitrate-hydrate $(Al(NO_3)_3 \cdot 9H_2O]$ were used as the precursor metal salts. The electrolytes used were 0.05 M aqueous solutions of $xAl(NO_3)_3 + (1 - x)ZrO(NO_3)_2$ with $x = 0.4$, 0.75 and 0.9. These electrolyte compositions aimed to represent the oxide compositions of ZrO_2–20 wt% Al_2O_3(ATZ), ZrO_2–42.6 wt% Al_2O_3 (eutectic composition) and ZrO_2–80 wt% Al_2O_3 (ZTA), respectively. The equivalent mole per cent concentrations of these alloys are presented in Table I. In the previous stages of the research, it was found that the most homogeneous and continuous deposits were obtained with ethanol additions of 25–50 vol % in water. Therefore, the volume ratio of water to ethanol was adjusted to 2:1 in the present electrolytes.

Coatings with different compositions were electrodeposited on TiC, TiB_2 and SiC bars of 3×20 mm. Prior to deposition, these substrates were mechanically polished with 600 grit SiC abrasive paper, rinsed with ethanol, washed with distilled water and dried in air. The electrical resistivities of the TiC, TiB_2 and SiC bars were 5×10^{-5}, 2×10^{-5} and 7 $\Omega\,cm^{-1}$, respectively.

The electrochemical setup has been described in detail in a previous publication [10]. Basically, two platinum anodes were used with a cathode centred between them. A galvanostatic regime was applied, and the temperature of the bath was kept at 10 °C, except in some experiments during which the temperature increased to 60 or 80 °C.

Electrodeposition was performed with no stirring at current densities of 5, 10 and 20 mA cm^{-2} and deposition durations of up to 60 min. The deposits were dried for 24 h in air at room temperature. Some of the specimens were sintered for 2 h at 900 °C either in air or within a closed graphite crucible (CO reducing atmosphere). The coating weight was determined by

0022–2461

TABLE I Comparative compositions within electrolytes and corresponding deposits

Electrolyte composition				Composition of deposit (mol %)[b]	
Actual (mol %)[a]		Designated (wt %)			
Al	Zr	Al_2O_3	ZrO_2	Al	Zr
40	60	20.0	80.0	73 ± 3	27 ± 3
75	25	57.4	42.6	82 ± 4	18 ± 4
90	10	80.0	20.0	80 ± 2	20 ± 2

[a] Standard deviation of ± 2.
[b] EDX results.

weighing the bar specimens before and after electrodeposition, within an accuracy of ± 0.05 mg. The thicknesses of the coatings were evaluated from scanning electron microscope images.

The microstructure of the as-deposited and the sintered coatings was characterized using a scanning electron microscope (SEM; Jeol, JSM-840) equipped with X-ray energy dispersive spectroscopy (EDX, model AN-10 000). X-ray diffraction (XRD) was used to determine the crystallinity as well as the phase content in the deposits. A diffractometer (model APD-1820) was operated at 40 kV and 40 mA, using monochromatized CuK_α radiation and a scanning speed of 0.4° min^{-1}.

Oxidation experiments were performed on a selected number of specimens, using a thermogravimetric analysis system (TGA model Setaram TGDTA92). The specimens were heated in air to 1100 °C at a heating rate of 10 °C min^{-1} and isothermally held for up to 24 h; weight changes being recorded during both stages. The net weight change during oxidation was determined by correcting the results relative to the changes observed for a blank-test platinum crucible. The exposed surface area of the coated test specimens was 0.9 cm^2.

3. Results

3.1. Electrodeposition on TiC substrates

The increase in the weight of the deposit versus the duration of deposition for constant electrolyte compositions is shown in Fig. 1. The weight of the deposit was found to increase with time up to ≈ 15, ≈ 6 and ≈ 8 min for $x = 0.4$, $x = 0.75$ and $x = 0.9$, respectively. At longer deposition durations, spallation resulted in a decrease of the weight of the deposit. The maximum weight of the deposit was higher in the Zr-rich solution ($x = 0.4$) relative to those in the "eutectic composition" ($x = 0.75$) or the Al-rich solutions ($x = 0.9$).

Corresponding cell voltages during electrodeposition experiments were recorded and shown in Fig. 2. The cell voltage increased continuously in the Zr-rich solution regardless of the maximum in the deposit weight. However, in other solutions, the increase in the cell voltage was more rapid, but reached a saturation level. The time at which the cell voltage saturated

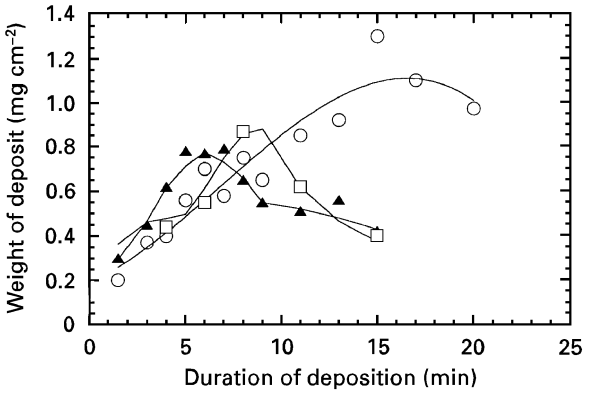

Figure 1 Deposit weight versus duration of deposition at 5 mA cm^{-2} and 10 °C on TiC substrates: (○) $x = 0.40$, (▲) $x = 0.75$, (□) $x = 0.90$.

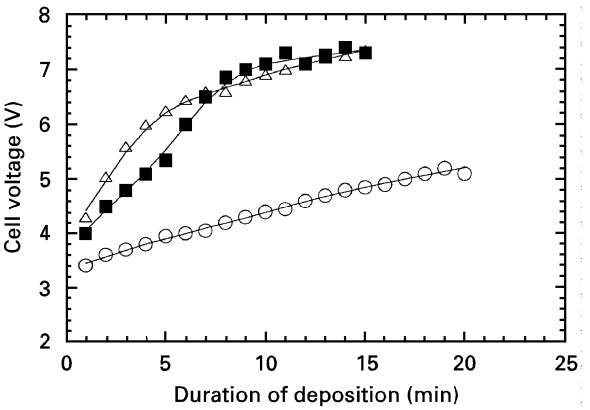

Figure 2 Cell voltage versus duration of deposition at 5 mA cm^{-2} and 10 °C on TiC substrates: (○) $x = 0.40$, (■) $x = 0.75$, (△) $x = 0.90$.

was comparable to the corresponding deposition duration at which the maximum deposit weight was recorded (Fig. 1). The cell voltages in the other solutions were higher than those measured for the Zr-rich solution ($x = 0.4$). These differences cannot be related to the electrical resistivities of the electrolyte solutions because comparable cell voltages were recorded for all the electrolytes, especially at the beginning of the electrodeposition. Therefore, the differences in the cell voltages are associated with the electrical resistivities of the growing deposits.

SEM observations (Fig. 3) show the smooth deposit surfaces which are typical for amorphous coatings. Microcracks are visible within the dried deposits as shown in Fig. 3a. These microcracks are most probably due to the stresses caused by the shrinkage on drying. According to the SEM observations, deposits up to 10 μm thick are formed. Experiments were conducted at higher temperatures in order to increase the green density of the deposit and thus inhibit microcracking. Owing to the low deposit weights at a current density of 5 mA cm^{-2}, the deposition experiments at 60 and 80 °C were performed at higher current densities. Fig. 4 shows the deposit weight versus the duration of deposition at a constant temperature of 80 °C and at current densities of 10 and 20 mA cm^{-2}. It is visible that at lower current density

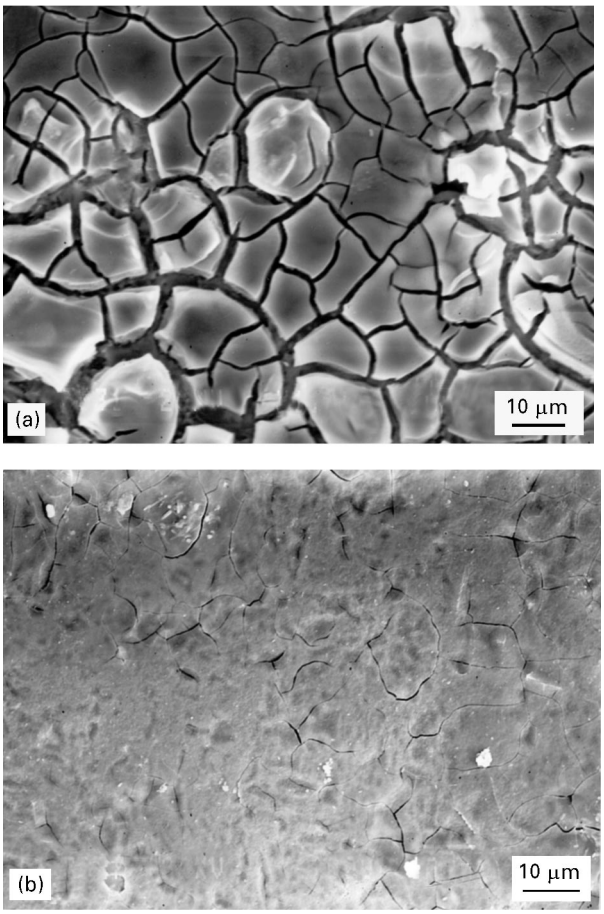

Figure 3 SEM images of green deposits on TiC substrates electrodeposited from an electrolyte with $x = 0.40$ in a bath at (a) 10 °C current density, 5 mA^{-1} cm^{-2}; duration, 7 min; deposit weight, 0.5 mg cm^{-2}, and (b) 80 °C; current density, 20 mA cm^{-2}; duration, 5 min; deposit weight, 0.5 mg cm^{-2}.

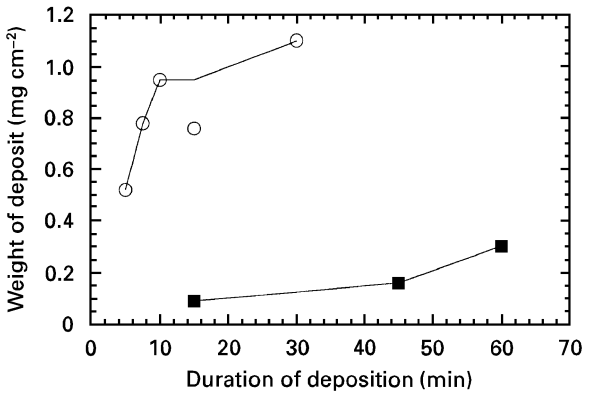

Figure 4 Deposit weight versus duration of deposition at 80 °C for $x = 0.40$ on TiC substrates. (○) 20 mA cm^{-2}, (■) 10 mA cm^{-2}.

of 10 mA cm^{-2}, relatively low deposit weights are recorded even for the very high deposition durations of 60 min. Nevertheless, at the higher current density of 20 mA cm^{-2}, the deposit weights are comparable to those measured for a current density of 5 mA cm^{-2} at 10 °C (compare with Fig. 1). Fig. 5 shows the deposit weight versus duration of deposition at a constant current density of 20 mA cm^{-2} at two different temperatures of 60 and 80 °C. Both curves indicate the formation of a continuous coating with no spallation.

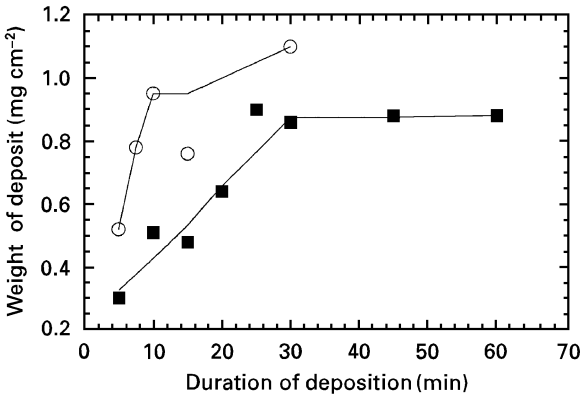

Figure 5 Deposit weight versus duration of deposition at 20 mA cm^{-2} and $x = 0.40$ on TiC substrates at (■) 60 °C and (○) 80 °C.

This was confirmed by the SEM image of the deposits formed at 80 °C, as shown in Fig. 3b. Although the 80 °C coating also contained microcracks, their extent and volume fraction were much lower than those in the coatings formed at 10 °C. Although the thicknesses of these specimens may differ, comparison of the two deposits (Fig. 3a and b) formed at different temperatures and current densities (but with similar deposit weights) reveals the effect of increasing bath temperature on enhancement of the density of the green deposit as well as on inhibition of microcracking within the deposits.

Finally, X-ray diffraction spectra of the as-deposited dried coatings have revealed two broadened peaks, regardless of the composition, of the deposit, which were typical for amorphous oxides.

3.2. Electrodeposition on TiB_2 substrates

Deposit weight and cell voltage versus duration of deposition in this system are shown in Figs 6 and 7, respectively. These dependencies are close to those found for the TiC substrates for the same electrolyte compositions. Similar differences exist between the deposit durations at which the maximum deposit weights are observed for the three different electrolyte compositions. Deposit weights obtained in the three different electrolytes using the TiB_2 substrates were higher than those obtained in corresponding experiments with TiC substrates; the differences were 20–30%. Higher cell voltages were also recorded on the TiB_2 substrates relative to the TiC substrates. The cell voltage steadily increased using the Zr-rich solution, but reached a saturation level for the other two electrolyte compositions. These results indicate the strong effect of electrolyte composition and hence of the composition of the deposit on the electrical resistance of the deposits.

3.3. Electrodeposition on SiC substrates

Owing to the lower electrical conductivity of the SiC substrates, the deposition experiments were conducted at a current density of 10 mA cm^{-2}. Maxima in the deposit weights were observed (Fig. 8) for deposition

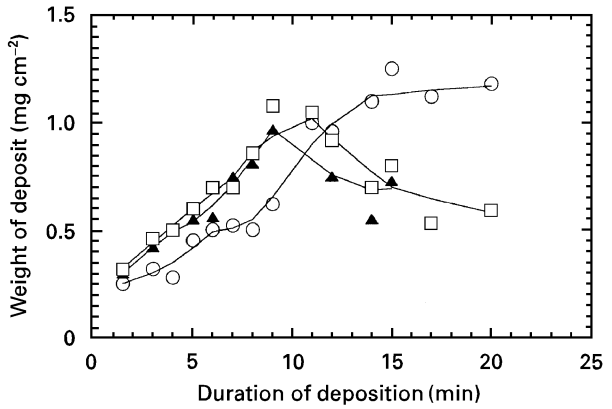

Figure 6 Deposit weight versus duration of deposition at 5 mA cm^{-2} and 10 °C on TiB_2 substrates: (○) $x = 0.40$, (▲) $x = 0.75$, (□) $x = 0.90$.

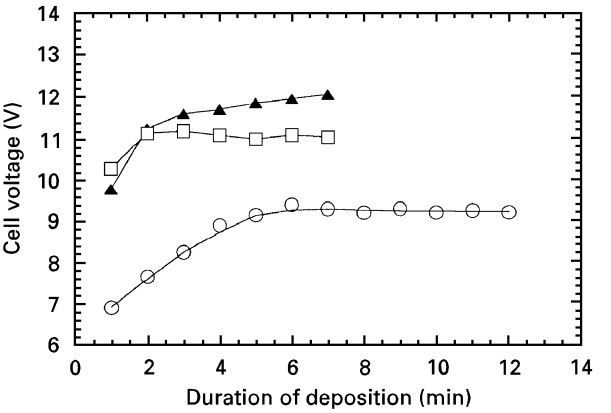

Figure 9 Cell voltage versus duration of deposition at 10 mA cm^{-2} and 10 °C on SiC substrates: (○) $x = 0.40$, (▲) $x = 0.75$, (□) $x = 0.90$.

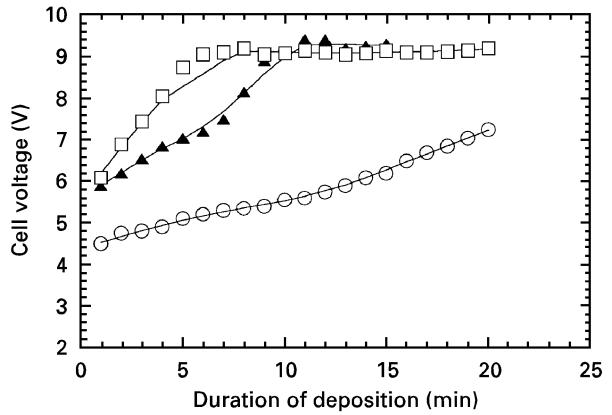

Figure 7 Cell voltage versus duration of deposition at 5 mA cm^{-2} and 10 °C on TiB_2 substrates: (○) $x = 0.40$, (▲) $x = 0.75$, (□) $x = 0.90$.

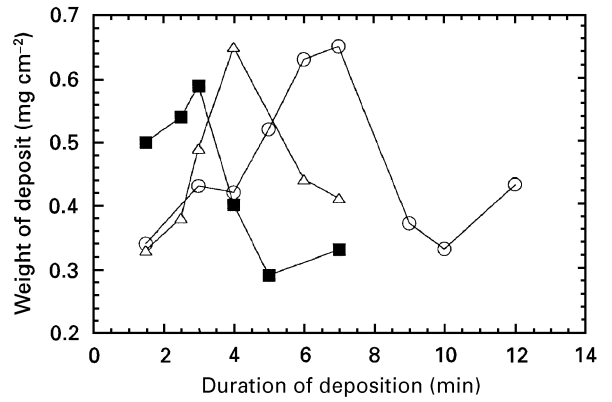

Figure 8 Deposit weight versus duration of deposition at 10 mA cm^{-2} and 10 °C on SiC substrates: (○) $x = 0.40$, (△) $x = 0.75$, (■) $x = 0.90$.

durations of 7, 4 and 3 min in solutions with $x = 0.4$, 0.75 and 0.9, respectively. These durations represent the maximal durations below which deposit spallation may be prevented. The deposit weights obtained on SiC substrates were significantly lower than those formed on TiC and TiB_2 substrates.

The cell voltage versus deposition duration dependencies (Fig. 9) were similar to those observed in the deposition experiments with TiC and TiB_2 substrates. Nevertheless, higher voltages were recorded for SiC substrates. In addition, the curves reached a saturation level for all the electrolyte compositions, in accordance with the time at which maxima were observed in the deposition weight versus duration curves (Fig. 8).

X-ray diffraction spectra of the as-deposited coatings have again shown two broadened peaks characteristic of the amorphous phase. Thus, the deposits were amorphous, independent of the substrate material and the electrolyte composition. The chemical compositions of the as-deposited coatings were characterized by EDX in SEM, using X-ray dot mapping with appropriate statistical treatment. These analyses were performed on islands of coating $\sim 10\,\mu m$ in diameter; the point step was corresponded to a spatial resolution (probe size) of $\sim 0.76\,\mu m$ with an acquisition time of 200 ms per point. Digitized mapping of Al (Fig. 10a) and Zr (Fig. 10b) as the coating elements and of Ti (Fig. 10c) as the substrate element revealed the non-homogeneous distribution of Al and Zr elements throughout the coating islands on the micrometer-size scale (Fig. 10). Quantitative compositional analysis by EDX (Table I) indicated that the average relative concentrations of Al and Zr in the deposits deviated significantly from those in their corresponding solutions. These results indicate that the deposition rate of Al-rich deposits is much higher than that of Zr-rich deposits.

In order to study the compositional homogeneity scale and level in these coatings, alumina–zirconia deposits ($x = 0.4$) were peeled from the TiC substrate and milled to powder for TEM observation. The powder particles always appeared featureless (Fig. 11a), characteristic of the amorphous phase. The amorphous nature of the deposit was verified by the diffuse ring on the electron diffraction pattern (Fig. 11b). This is in agreement with the XRD results of the green deposits. In addition, microchemical compositional analyses of the different powder particles (Table II) at very high magnification ($\times 50\,000$) shows a wide range of compositions, which verify compositional in-

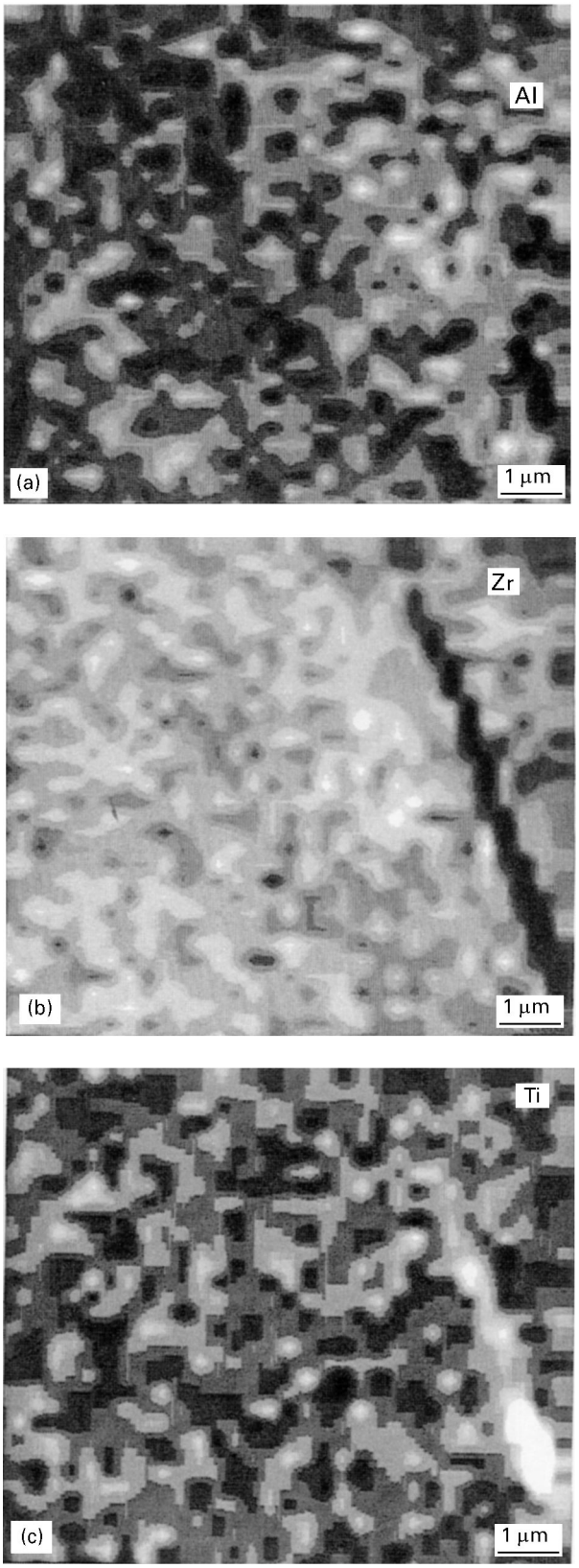

Figure 10 EDX digimap of (a) Al, (b) Zr and (c) Ti from an as-deposited coating ($x = 0.40$) on TiB_2 substrates.

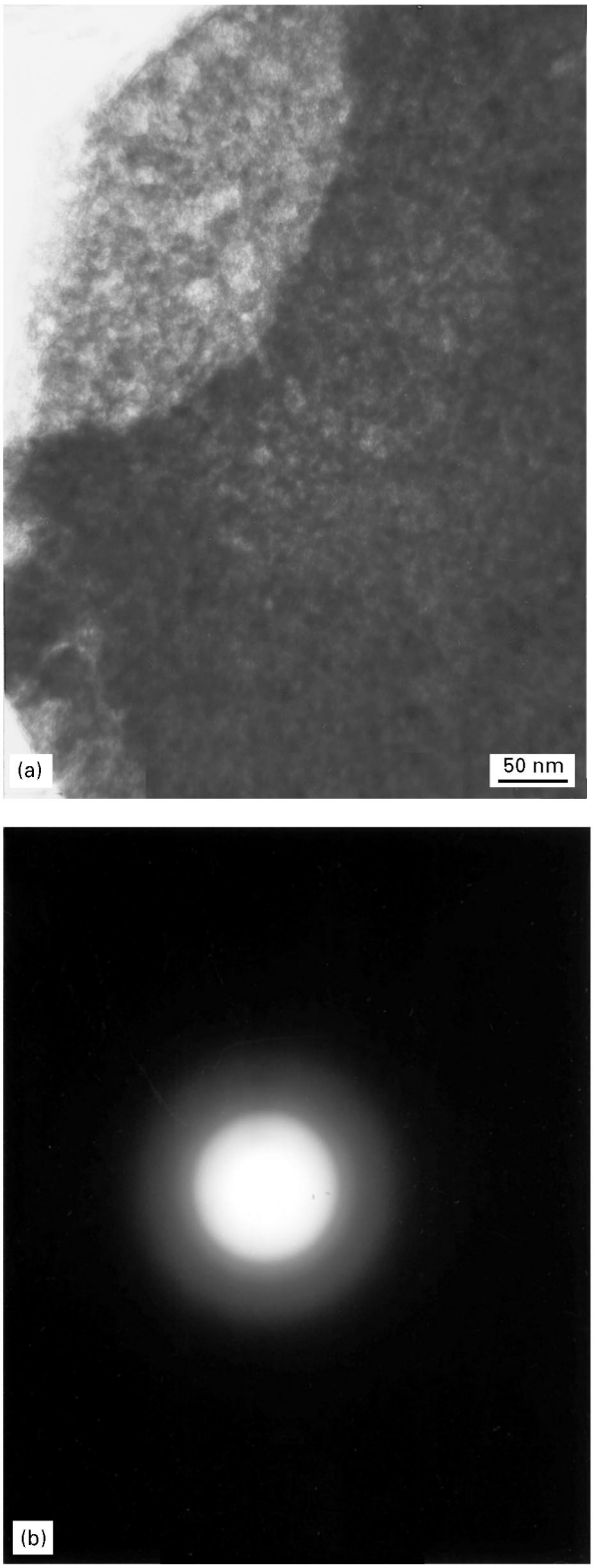

Figure 11 (a) Bright-field TEM image showing the featureless character of the amorphous deposit ($x = 0.40$). (b) Diffuse amorphous ring in the electron diffraction pattern from the area in Fig. 11a.

homogeneities within the deposits. Nevertheless, the low standard deviation of each composition, which resulted from three to five point analyses at different locations within the same powder particle, indicates that the chemical composition is fairly homogeneous at a submicrometre scale and below.

3.4. Sintered coatings

3.4.1. The alumina–zirconia–TiC system

Preliminary studies on air-sintering of the coatings on TiC substrates have shown significant oxidation and sublimation of the substrates. Therefore, this system was sintered within closed graphite crucibles. The microstructure of the sintered zirconia-rich–alumina

TABLE II EDX–TEM compositional results from powdered as-deposited alumina–zirconia coatings

Particle No.	Electrolyte composition[a]	Composition of deposit (wt %)	
		Al_2O_3	ZrO_2
1	0.4	64.8 ± 1.2	35.2 ± 1.2
2	0.4	38.7 ± 2.3	61.3 ± 2.3
3	0.4	28.5 ± 0.9	71.5 ± 0.9
4	0.9	94.1 ± 1.3	5.9 ± 1.3
5	0.9	89.9 ± 7.3	10.1 ± 7.3

[a] $x = 0.4$ refers to the compositon of Al_2O_3–80 wt % ZrO_2; $x = 0.9$ refers to the composition of Al_2O_3–20 wt % ZrO_2.

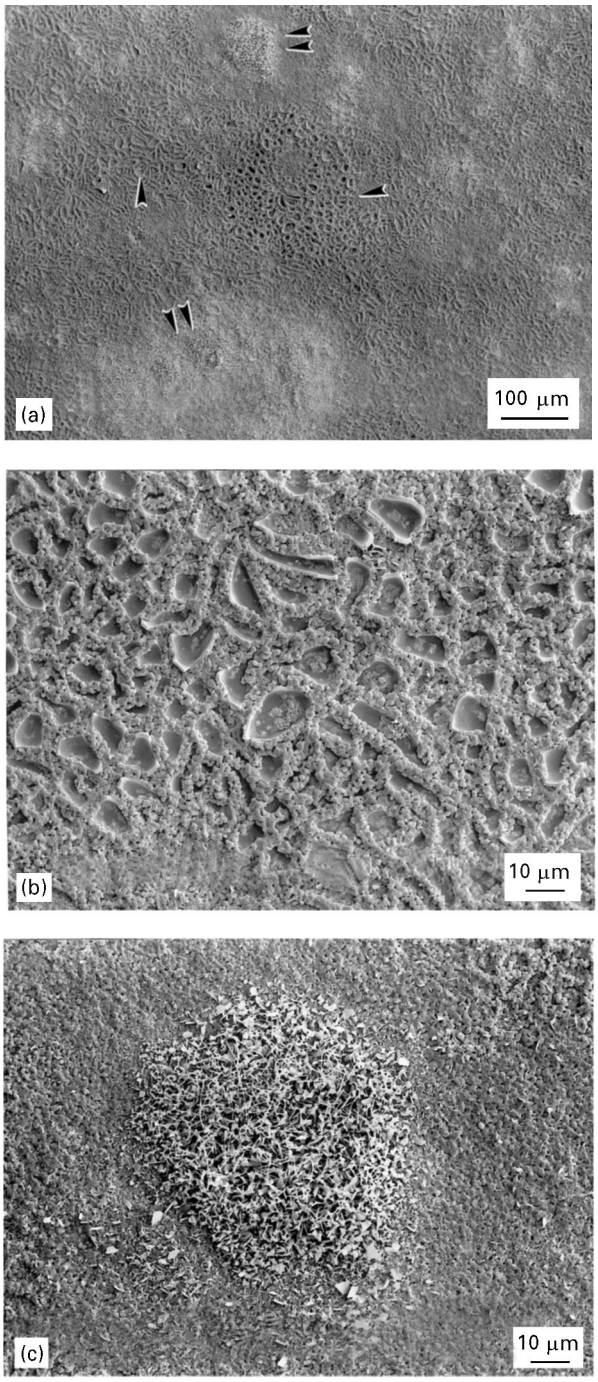

Figure 12 SEM images of the sintered Zr-rich deposits on a TiC substrate: (a) low magnification, (b) islands of coating surrounded by the growing polycrystalline titanium oxide (single arrows in Fig. 12 a) (c) whisker colonies at thin coating or deposit-free regions (double arrows in Fig. 12a).

coating ($x = 0.4$), shown by SEM, varied at different locations within the same specimen, depending on the thickness of the deposit (Fig. 12a). These microstructures were composed of either islands of deposit (in thick deposit regions) (Fig. 12b) and single-arrowed regions in Fig. 12a) or colonies of whiskers in thinner or deposit-free regions (Fig. 12c) and double-arrowed regions in Fig. 12a). The deposit islands were surrounded by micrometre-sized polycrystalline phases, most probably TiO_2 crystals that formed due to oxidation of the substrate. Further observation at higher magnifications showed the coating islands to have chemically reacted with the substrate, especially in their centres (Fig. 13a) (at sites where better contact exists between the coating and the substrate). The non-reacted regions of the deposit were composed of clusters of ultrafine grains as shown in Fig. 13b. The whiskers formed in the deposit-free or thin deposit regions exhibited a morphology characteristic of growth from the vapour phase (Fig. 13c). The exposed substrates revealed a microstructure similar to the polycrystalline phase that grew in the microcrack spaces between the deposit islands (Fig. 13d).

The sintered deposits with alumina–zirconia eutectic composition ($x = 0.75$) were found to be far more stable. A typical microstructure of these coatings at low magnification is shown in Fig. 14a and exhibits a homogeneous distribution of the sintered coating. Parts of the deposit islands were found to be debonded at their peripheries with the substrate, most possibly due to differential shrinkage during sintering. An SEM image at higher magnification (Fig. 14b) shows the shrinkage of the coating islands relative to their green states. Although the thermally etched surfaces of the surrounding substrate around the deposit islands exhibited a polycrystalline oxide, the islands did not react and were not covered with these crystals (as in the case of the Zr-rich deposits). For this coating composition, no chemical reaction was observed between the deposit islands and the substrate and no whiskers were formed even in very thin coating regions (Fig. 14c). The chemical compositions of the different microstructural features in these coatings were analysed by EDX–SEM and the results are summarized in Table III. These results are analysed in conjunction with the X-ray diffraction results from the same specimens in order to determine the phase contents and their relation to the microstructural features listed in Table III. The main difference between the Zr-rich and the eutectic deposits was the formation of zirconium titanates in the latter. These results will be discussed further.

The compositional homogeneity of the sintered deposits was characterized by EDX–SEM digimaps as described in Section 3.3. Fig. 15 shows the EDX digimap of the deposit island as well as part of the exposed substrate at microcrack spaces. While Ti and Al were found to be homogeneously distributed along the radius of the island, Zr was depleted in the periphery of the island. A similar trend was found in the other coating islands. This finding was supported by point analyses along the radii of the islands, the results of which are summarized in Table IV for two different islands.

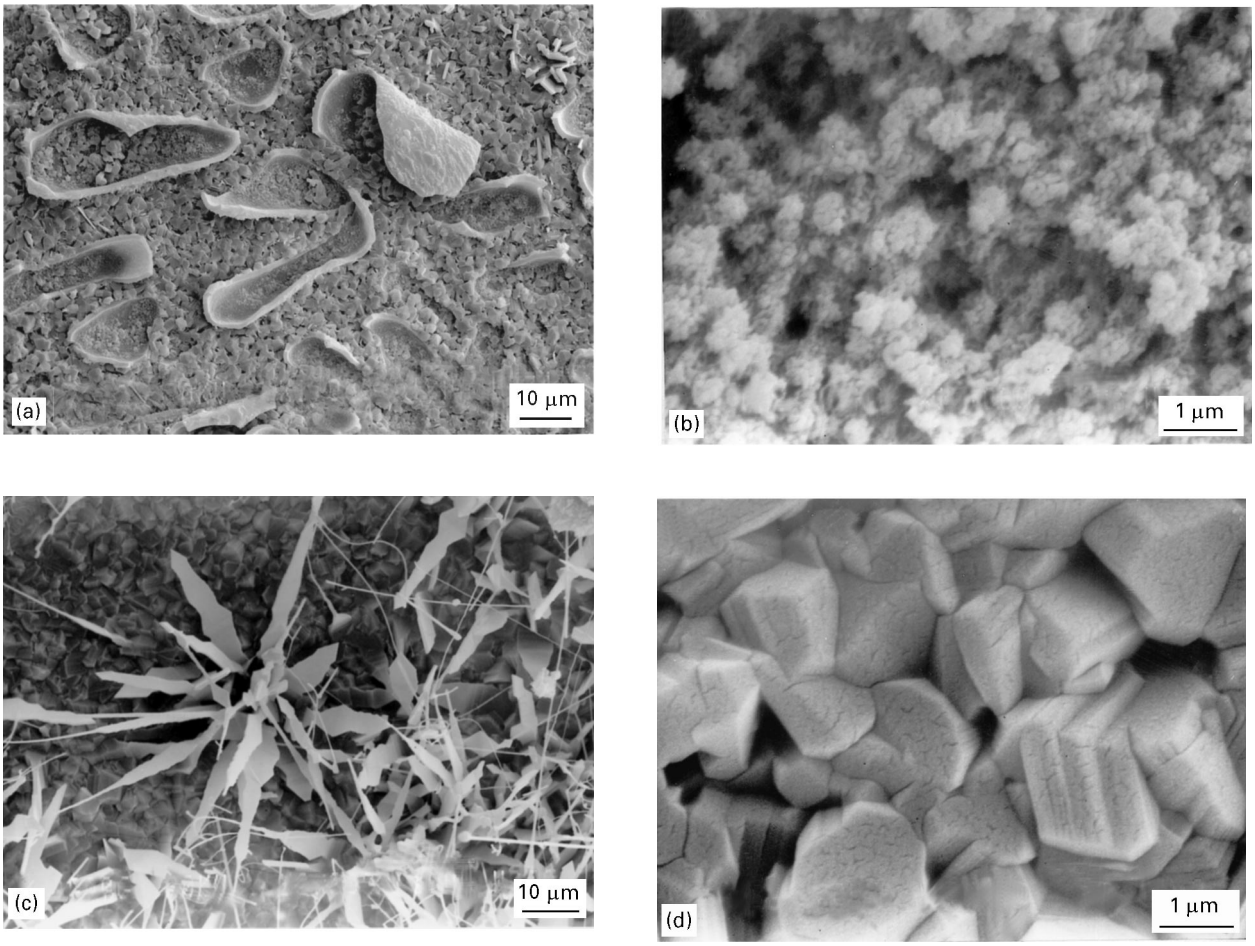

Figure 13 SEM images of the sintered Zr-rich deposits on TiC substrate: (a) deposit islands chemically reacted with the substrate grains, (b) ultrafine grained structure of the non-reacted deposit islands, (c) whisker morphology typical for growth from the vapour phase and (d) etched surfaces of the substrate.

3.4.2. The alumina–zirconia–SiC system

Similar SEM observations were performed on alumina–zirconia deposits ($x = 0.4$) on SiC substrates. However, in this system, no reaction was observed between the coating and the substrate; the deposit was chemically stable and adhered to the substrate (Fig. 16a). At high magnifications, the microstructure of the deposit was composed of clusters of ultrafine grains, especially in thicker coating regions (Fig. 16b). At thinner coating regions, the deposit was smooth and continuous, except for some fine microcracks at thicker locations (arrowed in Fig. 16c). EDX chemical composition analysis of the coating showed a higher alumina content (61.2 wt %) relative to those found in the same deposits (34.3 wt %) on TiC substrates. However, this fact may be attributed to the contribution of the X-ray yield of silicon (k line) from the substrate to the aluminum (k line) peak.

The X-ray diffraction spectrum showed the presence of SiC, Si, SiO_2, α-alumina and traces of monoclinic ZrO_2 in the specimen. This phase evolution is consistent with the oxidation of SiC to SiO_2 at exposed regions between the islands of deposit. In addition, limited solid solubility between zirconia and alumina is expected to lead to phase separation into pure oxide constituents during sintering.

3.5. Oxidation resistance

Two specimens each with a deposit weight of $\sim 1.30\ mg\ cm^2$, were used for the oxidation studies. The increase in weight during oxidation at 1100 °C for ATZ coatings ($x = 0.4$) on TiC and TiB_2 substrates is shown in Fig. 17a and Fig. 17b, respectively. Both systems exhibit a parabolic oxidation behaviour, which may be considered as the passive oxidation regime (formation of protecting TiO_2 layer). However, the oxidation kinetics of the coated TiC substrate is significantly lower relative to that of the non-coated substrate (Fig. 17a). From the slope of the oxidation curves it can be deduced that at longer oxidation durations, the difference in the weight change between coated and non-coated specimens may only increase. This fact indicates efficient oxidation protection of the TiC substrate by the alumina–zirconia coating. On the other hand, oxidation behaviours of the coated and non-coated TiB_2 substrates are fairly similar (Fig. 17b). Thus, no oxidation protection was achieved for the TiB_2 substrates with alumina–zirconia coatings. These results may be rationalized with respect to the chemical reactions in each system as will be discussed below.

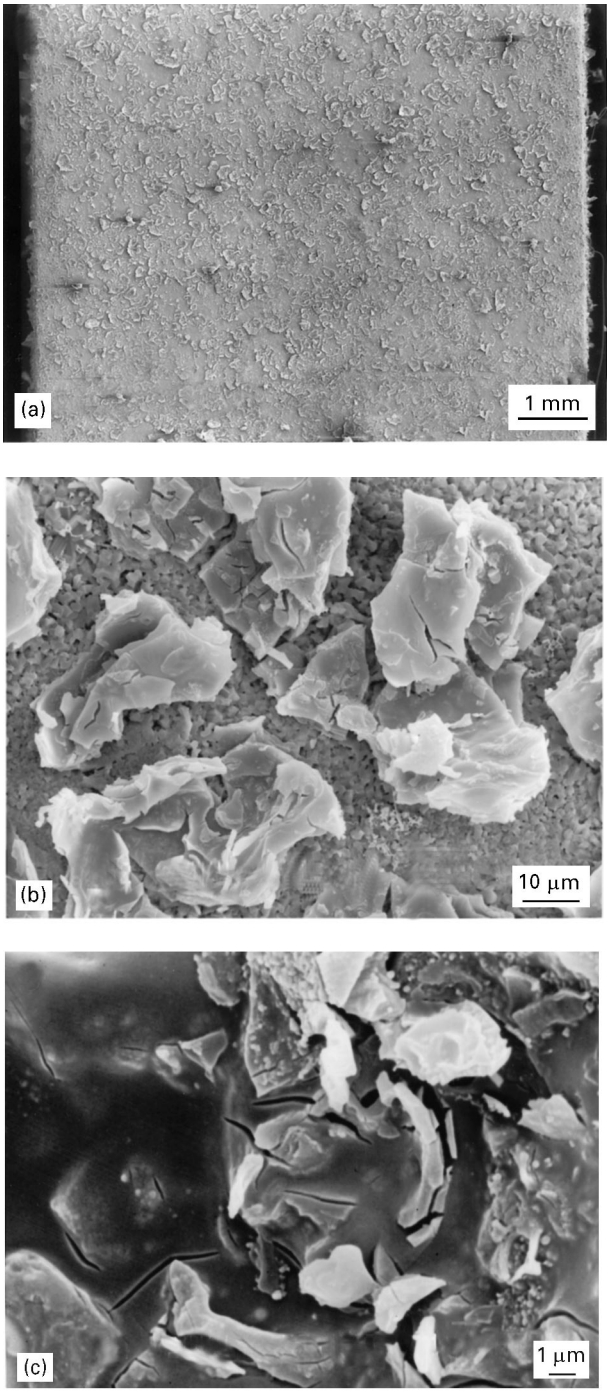

Figure 14 SEM images showing (a) partial debonding of the deposit islands ($x = 0.75$) from the TiC substrate, (b) lack of reaction between the deposit and the substrate, and the (c) thin coating region.

4. Discussion

The equilibrium alumina–zirconia phase diagram is known to exhibit negligible solid solubility between alumina and zirconia. However, several workers [16–21] reported formation of extended solid solutions via liquid precursors. With respect to Zr-rich compositions, Yamaguchi and coworkers [16, 17] reported formation of amorphous solid solutions with compositions of up to 45 mol % Al_2O_3 by the alkoxide route. They also reported partitioning of the solid solutions into cubic zirconia at low temperatures and to tetragonal and α-alumina above 970 °C. Balmer *et al.* [18, 19] reported formation of amorphous solid solutions in Zr-rich compositions (up to 40 mol % Al_2O_3) by pyrolysis. They found that phase evolution at high temperatures was associated with crystallization of solid solutions into metastable phases, such as tetragonal zirconia and γ-alumina, which in turn transformed into more stable phases, such as monoclinic zirconia and α-alumina.

A mixture of an aluminum oxy-hydroxide gel solid solution and amorphous zirconia was reported to exist in the Al-rich side (above 10 mol % ZrO_2) [20]. Using the alkoxide route, Boulton *et al.* [21] have prepared Al-rich solid solutions up to the eutectic composition. No crystalline phases of Al_2O_3 were detected below 1100 °C.

These results indicate that amorphous alumina–zirconia alloys may be formed by wet chemical processes. Considering the role of anions in hydrolysis and condensation of the inorganic precursor, Zhang and Glasser [22] have shown that nitrate ions (NO_3^-) can co-ordinate with aluminum or zirconium atoms. On the other hand, Livage *et al.* [23] found NO_3^- to be a weakly complexing anion with zirconium. Thus, NO_3^- ions may be adsorbed on the surfaces of the aluminum and zirconium ions formed by dissolution of the nitrate salts. Nevertheless, at the high pH values obtained at the cathodic surfaces, NO_3^- may be released resulting in condensation of amorphous hydrous zirconia–alumina deposits. Indira and Kamath [24] claim that the compositions of the binary hydroxides electrodeposited from mixed nitrate solutions were close to that of the solutions if the two metal hydroxides had comparable solubility products.

Condensation–polymerization of aluminum–zirconium oxy-hydroxides from their mixed nitrates under conditions of decreasing acidity was investigated by Zhang and Glasser [22]. Using the partial charge model calculations, they found that in mixed Al–Zr gel systems, Al^{3+} does not participate in the initial polymerization, but decomposes into low polymer species. Zr^{4+} was found to control the polymerization rate of the mixture. Their nuclear magnetic resonance (NMR) studies have shown that Al^{3+} does not copolymerize with zirconium but, instead, higher molecular weight polymers of aluminum decompose to lower molecular weight units. The implications of these findings are that such aluminum–zirconium oxy-hydroxide products may be composed of ultrafine Al- and Zr-rich grains. The compositional characteristics of the as-deposited coatings are in good agreement with these models.

In order to estimate quantitatively the effect of the electrolyte composition on the deposition rate, we will consider the reactions occurring in the present system. The hydroxyl may be formed by different reactions, such as solvent reduction

$$H_2O + 2e^- \Rightarrow H_2 + (OH)^- \quad (1)$$

or electrolyte reduction

$$H_2O + NO_3^- + 2e^- \Rightarrow NO_2^- + 2(OH)^- \quad (2)$$

$$\vdots \quad \vdots \quad \vdots \quad \vdots \quad \vdots$$

$$6H_2O + NO_3^- + 8e^- \Rightarrow NH_3 + 9(OH)^- \quad (3)$$

TABLE III Chemical composition and phase content of sintered alumina–zirconia coatings on TiC substrates

Composition	Microstructural feature	Composition (wt %)		
		Al_2O_3	ZrO_2	TiO_2
$x = 0.4$[a]	Deposit islands	34.3 ± 3.2	65.7 ± 3.2	–
	Whiskers	–	21.3 ± 3.6	78.7 ± 3.6
	Substrate	–	27.3 ± 1.2	72.7 ± 1.2
$x = 0.75$[b]	Deposit islands	59.7 ± 9.5	40.3 ± 9.5	–

[a] Phase content as determined by XRD: α-Al_2O_3, TiO_2, TiC, Al_2TiO_5.
[b] Phase content as determined by XRD: α-Al_2O_3, TiO_2, TiC, Al_2TiO_5, $ZrTiO_4$, $Zr_{0.5}Ti_{0.5}O_{0.33}$.

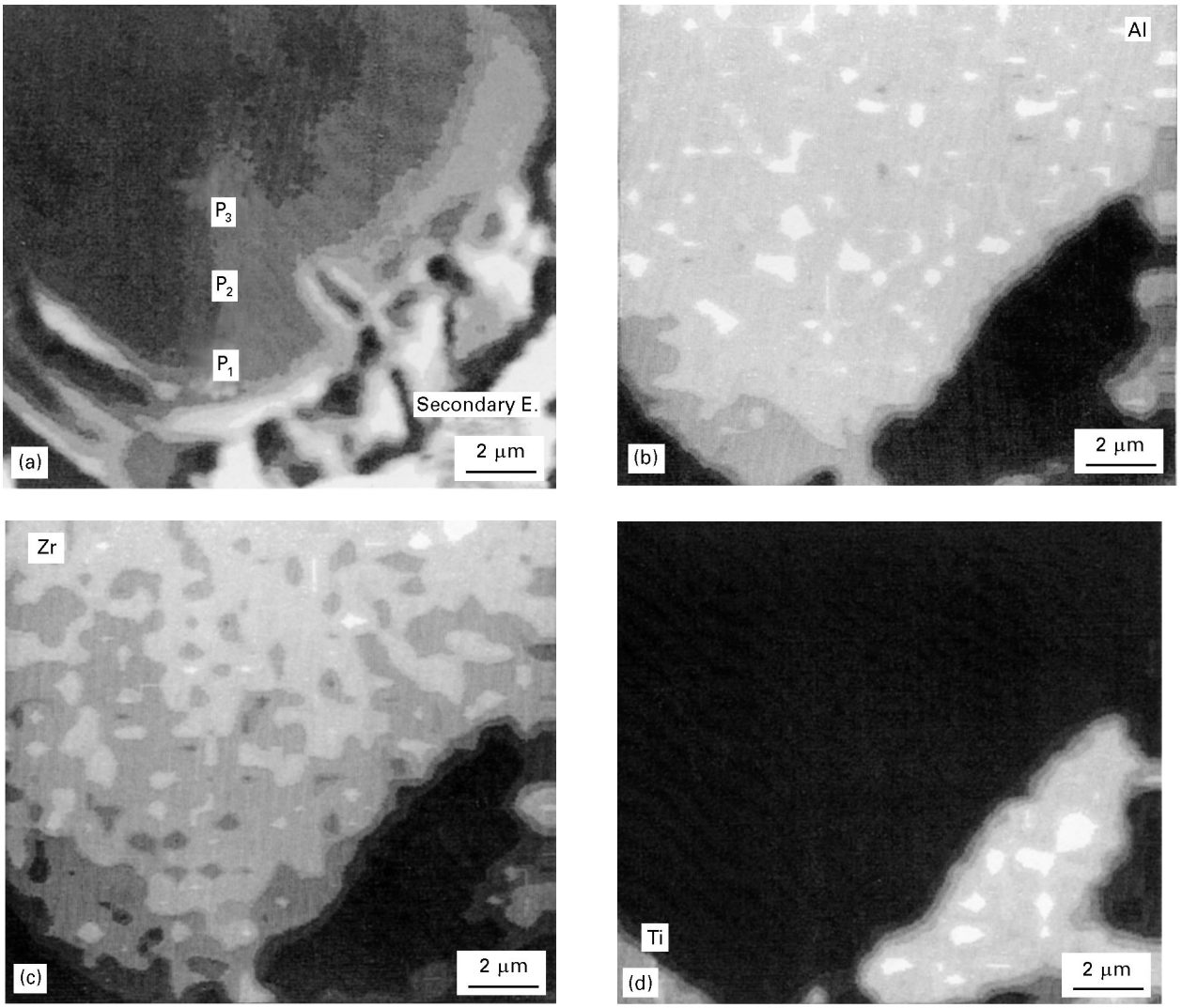

Figure 15 EDX digimap of (a) secondary electrons, (b) Al, (c) Zr and (d) Ti from the periphery of an as-sintered coating island ($x = 0.40$) on TiC substrate.

All the reactions between Equations (2) and (3) produce hydroxyl ions approximately in the ratio of 1:1 of e^- to $(OH)^-$. Thus, assuming that the reduction of nitrate (Equation 3) is the main source for formation of hydroxyls [23] and that all the hydroxyls are used to form the hydroxide, Streinz *et al.* [25] calculate the deposition rate of $Ni(OH)_2$ from a nitrate solution using Faraday's law.

In order to apply this approach to the aluminum–zirconium hydroxide system, we assume that all the available Al^{3+} and Zr^{4+} cations near the cathode equally react (100% efficiency) with the hydroxyl groups generated at the cathode, to form the hydroxides. Another assumption is that the electrolyte composition does not change during electrodeposition. These hydroxides form according to the following reactions

$$Al^{3+} + 3(OH)^- \Rightarrow Al(OH)_3 \quad (4)$$

$$Zr^{4+} + 4(OH)^- \Rightarrow Zr(OH)_4 \quad (5)$$

TABLE IV Chemical composition of sintered alumina–zirconia coatings ($x = 0.4$) on TiC substrates

Island No.	Point No.	Location	Composition (wt %)	
			Al_2O_3	ZrO_2
1[a]	P_1	Periphery	75.6	24.4
	P_2	Midway	70.7	29.3
	P_3	Centre	69.7	30.3
2	P_1	Periphery	78.4	21.6
	P_2	Midway	76.2	23.8
	P_3	Midway	70.5	29.5
	P_3	Centre	67.1	32.9

[a] See Fig. 15.

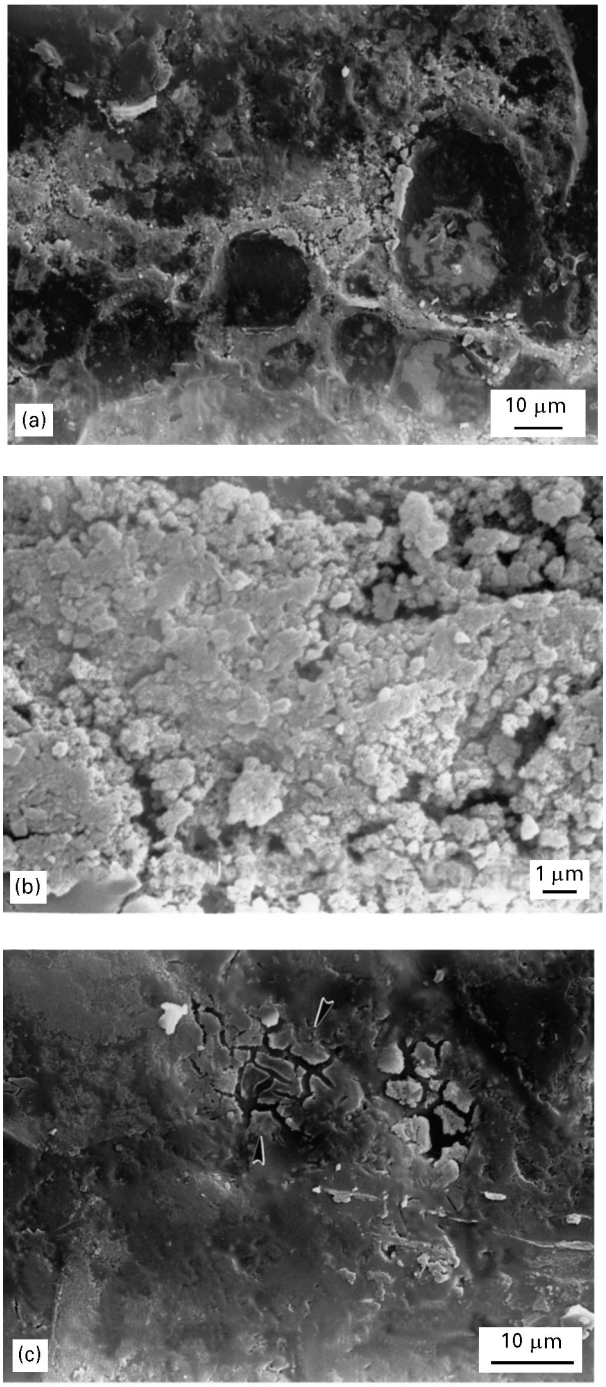

Figure 16 SEM images of the sintered alumina–zirconia deposits ($x = 0.40$) on SiC substrate: (a) low-magnification, (b) ultrafine grain clusters of the deposit, and (c) thin coating region.

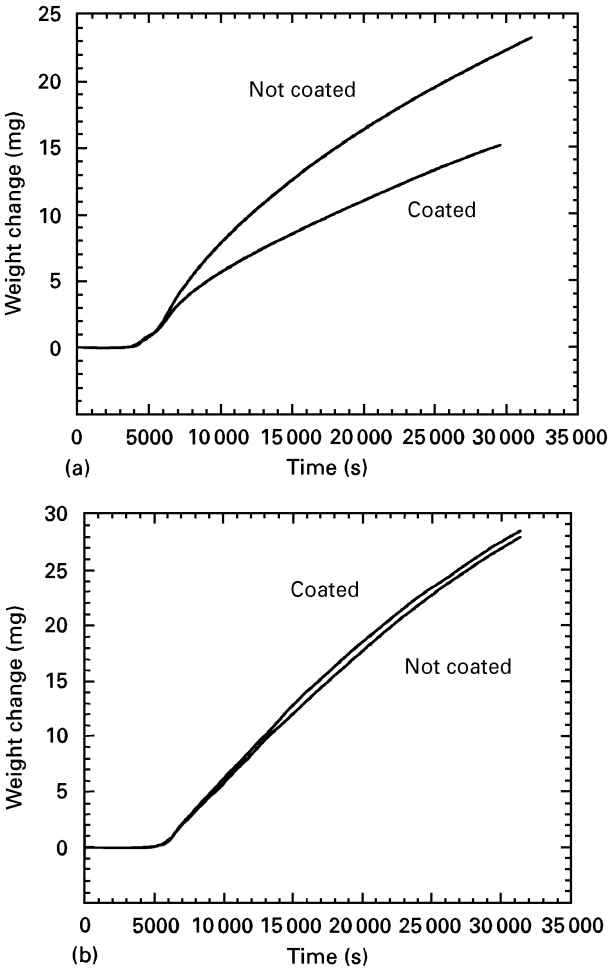

Figure 17 Oxidation curves of (a) TiC and (b) TiB_2 substrates with and without alumina–zirconia coatings ($x = 0.40$) at 1100 °C in air.

The deposition rate ($g\,s^{-1}$) of the alloy-composite hydroxide may be written as (see the appendix)

$$dm/dt = (AI/F) \times \{(3x/8) \times M_{Al(OH)_3} + [9(1-x)/32] \times M_{Zr(OH)_4}\} \quad (6a)$$

where A is the cathode area, I is the current density, F is Faraday's constant, x is the volume fraction and M is the molecular weight. Neglecting the contribution of the absorbed water in the dried deposits to their molecular weight, we use $M_{Al(OH)_3} = 78\ g\,mol^{-1}$ and $M_{Zr(OH)_4} = 159.22\ g\,mol^{-1}$ for our calculations. Using the following values: $A = 2.5\ cm^2$, and $F = 96\,487$ C, we have calculated the expected deposition rates for different electrolyte compositions and current densities. These results together with their corresponding experimental deposition rates are summarized in Table V. The calculated results are higher, but in the same order of magnitude as the experimental data, and show a continuous decrease in the deposition rate with increasing aluminum content of the electrolyte. Nevertheless, comparison with the measured data reveals that the deposition efficiency is relatively low regardless of the substrate material. The reason for the increase in the experimental deposition rate for the eutectic composition on TiC ($x = 0.75$) is not known. The effect of the substrate material on deposition rate may be related to the degree of ad-

TABLE V Theoretical and experimental electrodeposition rates in codeposition of alumina–zirconia from their nitrate solutions

	Calculated dm/dt (mg min^{-1})[a]		Measured dm/dt (mg min^{-1})			
x	5 mA cm^{-2}	10 mA cm^{-2}	5 mA cm^{-2} TiB_2	5 mA cm^{-2} TiC	10 mA cm^{-2} SiC	Remarks
0.00	0.35	0.70	–	–	0.50[b]	Al-free
0.40	0.30	0.60	0.12	0.17	0.14	–
0.75	0.26	0.51	0.20	0.32	0.30	–
0.90	0.24	0.48	0.20	0.21	0.17	–
1.00	0.23	0.45	–	–	0.13[b]	Zr-free

[a]Using Equation 6A.
[b]Reference [5].

hesion between the deposit and the substrate. Substrates with high electrical conductivity and inert to hydrogen bonds will exhibit poor adhesion with the deposit, and will lead to sedimentation of a powdery precipitate. Increase in the covalency of the substrate material from $TiC \Rightarrow SiC \Rightarrow TiB_2$ is expected to lower their tendencies to form hydrogen bonds with the deposit. The relatively low deposition rates observed at higher current densities may be due to evolution of hydrogen gas, which disturbs the process of deposition build-up.

Increase in the temperature of the bath was found to decrease the extent of microcracking, probably by increasing the density of the deposit. The temperature effect should be considered through the behaviour of the electrolyte and especially the change in the dielectric constant of the solvent as well as the diffusivity of the solute ions. The lower the dielectric constant of the medium, the higher the electrostatic attraction between the ions and thus the higher the tendency for precipitation. The dielectric constant of the present solvent (water:ethanol in 2:1 ratio) is ≈ 59 at 25 °C [26]. Increase in temperature is expected to lower this value to 47 at 80 °C, which is far above the critical value (≈ 25) needed for precipitation [27]. This indicates a negligible effect of the temperature via the electrolyte's dielectric constant on the deposition rate. On the other hand, the temperature increase is also expected both to lower the electrolyte viscosity and increase the diffusivity of the ionic species to the cathodic surfaces. Formation of denser deposits at higher temperatures may be a manifestation of the latter effects.

With respect to microstructural and compositional evolution in these coating–substrate systems one can point to the crucial effect of Zr on the formation of both stoichiometric ($ZrTiO_4$) and substoichiometric zirconium titanates ($Zr_{0.5}Ti_{0.5}O_{0.33}$) at coating–substrate interfaces, which are associated with chemical reaction between the coating and the substrate. In the case of coatings with eutectic composition that are richer in alumina content, the chemical reaction is less favourable due to the need to form a stoichiometric aluminum titanate compound (Al_2TiO_5). The whiskers are most probably TiO_2 formed by an evaporation–condensation mechanism due to the high partial pressure of TiO_2 at 900 °C.

The difference in the oxidation behaviour of the two systems may be understood with respect to phase evolution at high temperatures in these systems. In the alumina–zirconia coating on TiB_2 substrates, oxidation of TiB_2 is expected to form boric oxide (B_2O_3), which is already a melt around 450 °C. Such phase evolution was observed in the chromia coating–TiB_2 substrates [7]. The presence of the liquid phase is expected to enhance the oxidation kinetics due to much higher diffusion rates of the ionic species through the oxide layer.

Appendix A

The electrochemical deposition rate of a monolithic hydroxide from the electrolyte on the cathode substrate may be determined using Faraday's law

$$dm/dt = (m/n) \times (IAM/ZF) \quad \text{(A1)}$$

where dm/dt is the deposition rate (g s^{-1}), I is the applied current density (A cm^{-2}), A is the electrode area (cm^2), M is the molecular weight of the deposit, Z is the valency of the hydroxide's cation, F is the Faraday constant, and the m/n ratio indicates that m moles of hydroxyl that are formed by n charges are needed to produce (m/n) moles of the hydroxide.

Because the applied current density is often far above the exchange current density, one should consider the effect of the overvoltage on the current density using the Tafel equation

$$-I = I_0 \exp[(-\alpha ZF/RT)\eta] \quad \text{(A2)}$$

where I_0 is the exchange current density, α is the transfer coefficient ($0 < \alpha < 1$), η is the overvoltage, R is the gas constant, and T is the temperature.

Thus using Equations (A1) and (A2), the deposition rate may be written in the explicit form of

$$dm/dt = (m/n) \times (AM/ZF) \times I_0 \exp[(-\alpha ZF/RT)\eta] \quad \text{(A3)}$$

Electrodeposition of the alloy–composite hydroxides was made possible using mixed electrolyte solutions of their salts. Because the electrochemical behaviour of the mixed system is an additive property of its original constituents, the deposition rate in Equation (A3) may be expanded as a summation over the j constituents in the system

$$dm/dt = (A/F) \times (m/n) \Sigma (X_j M_j/Z_j) \times I_0 \exp[(-\alpha_j Z_j F/RT)\eta_j] \quad \text{(A4)}$$

where X_j is the volume fraction of the j constituent.

TABLE AI Ionic diffusion coefficients at 25 °C and infinite dilution, D

Ion	NO_3^-	OH^-	$1/3Al^{3+}$	$1/4Zr^{4+}$
$D \times 10^{-5}$ ($cm^2\ s^{-1}$)	1.902	5.273	0.541	0.45–0.78

At this stage one should identify the rate-controlling species in the electrodeposition process. With respect to the cathodic polarization curves for zirconyl nitrate and aluminum nitrate solutions with SiC electrodes [5], one may conclude that the present applied current densities (i.e. 5, 10 and 20 mA cm^{-2}) are in the concentration polarization regime, and above the limiting (diffusion) current densities. Therefore, diffusion coefficients of the different ionic species that exist in the system were compiled [26] as listed in Table AI.

Because most diffusion coefficients of the metal cations fall within the narrow range of 0.45×10^{-5} to $0.78 \times 10^{-5}\ cm^2\ s^{-1}$, we will assume the diffusion coefficient of Zr^{4+} to be within this range. It is visible from Table AI, that the diffusivities of Zr^{4+} and Al^{3+} are lower by a factor of 2–4 from that of the nitrate ion, and by an order of magnitude from that of the hydroxyl ions. Therefore, formation of the metal hydroxide must possibly occur in the solution, outside the concentration layer, by rapid diffusion of the hydroxyl ions from the surfaces of the cathode. Once polynuclear species of the hydroxide are formed, they migrate towards the cathode by electrophoretic forces.

Thus formation of the aluminum and zirconium hydroxides is not controlled by diffusion of their cations through the double layer, but is directly proportional to the applied current. Formation of a continuous hydroxide deposit having lower electrical conductivity than that of the cathode over which it is deposited, is expected to decrease the efficiency of the current of formation of the hydroxyl ions at the cathode. However, this will cause, simultaneously, an increase in the voltage drop across the cell, and an increase in the electrophoretic forces, i.e. the probability of formation of hydroxide species deposited onto the cathode. The net effect is the decrease in the deposition rate to zero. In conclusion, the appropriate electrodeposition rate for the conditions of the present study may be written as

$$\mathrm{d}m/\mathrm{d}t = (AI/F) \times (m/n) \times \{(x/3) \times M_{Al(OH)_3} + [(1-x)/4] \times M_{Zr(OH)_4}\} \quad \text{(A5)}$$

In order to apply this approach we assume that all the available Al^{3+} and Zr^{4+} cations near the cathode react equally (100% efficiency) with the hydroxyl groups generated at the cathode, to form the hydroxides. Another assumption is that the electrolyte composition does not change during the electrodeposition. The m/n ratio is 9/8 for both hydroxides with respect to Equation 3. Thus Equation A5 may be presented as

$$\mathrm{d}m/\mathrm{d}t = (AI/F) \times \{(3x/8) \times M_{Al(OH)_3} + [9(1-x)/32] \times M_{Zr(OH)_4}\} \quad \text{(A6)}$$

This equation is applicable to the linear portion of the deposition weight versus the duration of deposition curves (low current densities and durations) that exists before the maxima at which spallation occurs.

Acknowledgements

This research was supported by a grant of the Ministry of Science and the Arts and of Forschungszentrum Juelich GmbH (KFA)-Projecktttraeger fuer Biologie, Material und Rohstofforschung (PLR) Germany. Dr A. Berner is acknowledged for performing the digimap analyses.

References

1. J. A. SWITZER, *Bull. Amer. Ceram. Soc.* **66** (1987) 1521.
2. J. A. SWITZER and R. J. PHILIPS, *Proc MRS Symp.* **121** (1988) 111.
3. L. GAL-OR, I. SILBERMAN and R. CHAM, *J. Electrochem. Soc.* **138** (1991) 1939.
4. R. CHAIM, I. SILBERMAN and L. GAL-OR, *ibid.* **138** (1991) 1942.
5. R. CHAIM, G. STARK, L. GAL-OR and H. BESTGEN, *J. Mater. Sci.* **29** (1994) 6241.
6. *Idem, J. Mater. Sci. Lett.* **13** (1994) 487.
7. R. CHAIM, S. ALMALEH-ROCKMAN, L. GAL-OR and H. BESTGEN, *J. Amer. Ceram. Soc.* **78** (1995) 3202.
8. L. INDIRA, M. DIXIT and P. V. KAMATH, *J. Power Sources* **52** (1994) 93.
9. G. SASIKALA, S. MOORTHY BABU and R. DHANASEKARAN, *Mater. Chem. Phys.* **42** (1995) 210.
10. J. WANG and R. STEVENS, *J. Mater. Sci.* **23** (1988) 804.
11. R. CHAIM, *ibid.* **27** (1992) 5597.
12. J. WANG and R. STEVENS, *ibid.* **24** (1989) 3421.
13. Y. MATSUMOTO, K. HIROTA, O. YAMAGUCHI, S. INAMURA, H. MIYAMOTO, N. SHIOKAWA and K. TSUJI, *J. Amer. Ceram. Soc.* **76** (1993) 2677.
14. E. L. COURTRIGHT, J. S. HAGGERTY and J. SIGALOVSKY, *Ceram. Eng. Sci. Proc.* **14** (1993) 671.
15. S. C. FARMER and A. SAYIR, *ibid.* **16** (1995) 1101.
16. O. YAMAGUCHI, M. SHIRAI and M. YOSHINAKA, *J. Amer. Ceram. Soc.* **71** (1988) C-510.
17. D. INAMURA, H. MIYAMOTO, Y. IMAIDA, M. TAKAGAWA, K. HIROTA and O. YAMAGUCHI, *J. Mater. Sci.* **29** (1994) 4913.
18. M. L. BALMER, F. F. LANGE and C. G. LEVI, *J. Amer. Ceram. Soc.* **77** (1994) 2069.
19. M. L. BALMER, F. F. LANGE, V. JAYARAM and C. G. LEVI, *ibid.* **78** (1995) 1489.
20. K. YAMAKATA, K. HIROTA, O. YAMAGUCHI, H. KUME, S. INAMURA and H. MIYAMOTO, *ibid.* **77** (1994) 2207.
21. J. M. BOULTON, S. SUBRAMONEY and D. R. UHLMANN, in "Ultrastructure processing of advanced materials", edited by D. R. Uhlmann and D. R. Ulrich (Wiley, New York, 1992) p. 385.
22. W. ZHANG and F. P. GLASSER, *J. Mater. Sci.* **28** (1993) 1129.
23. J. LIVAGE, M. CHATRY, M. HENRY and F. TAULELLE, *Proc. MRS Symp.* **271** (1992) 201.
24. L. INDIRA and P. V. KAMATH, *J. Mater. Chem.* **4** (1994) 1487.
25. C. C. STREINZ, A. P. HARTMAN, S. MOTUPALLY and J. W. WEIDNER, *J. Electrochem. Soc.* **142** (1995) 1084.
26. R. C. WEST (editor), "Handbook of chemistry and physics" (CRC Press, Boca Raton, FL, 1989) pp. 5–90.
27. Y. T. MOON, H. K. PARK, D. K. KIM, C. H. KIM and I.-S. SEOG, *J. Amer. Ceram. Soc.* **78** (1995) 2690.

Received 27 February
and accepted 17 July 1996